GEOPHYSICS, VOL. 71, NO. 3 (MAY-JUNE 2006); P. C15–C24, 4 FIGS., 3 TABLES.
10.1190/1.2194896

Use of AVOA data to estimate fluid indicator in a vertically fractured medium

Ranjit K. Shaw[1] and Mrinal K. Sen[2]

ABSTRACT

Microstructural attributes of cracks and fractures, such as crack density, aspect ratio, and fluid infill, determine the elastic properties of a medium containing a set of parallel, vertical fractures. Although the tangential weakness Δ_T of the fractures does not vary with the fluid content, the normal weakness Δ_N exhibits significant dependence on fluid infill. Based on linear-slip theory, we used the ratio $g\Delta_N/\Delta_T$ — termed the fluid indicator — as a quantitative measure of the fluid content in the fractures, with g representing the square of the ratio of S- and P-wave velocity in the unfractured medium. We used a Born formalism to derive the sensitivity to fracture weakness of PP- and PS-reflection coefficients for an interface separating an unfractured medium from a vertically fractured medium. Our formulae reveal that the PP-reflection coefficient does not depend on the 2D microcorrugation/surface roughness with ridges and valleys parallel to the fracture strike, whereas the PS-reflection coefficient is sensitive to this microstructural property of the fractures. Based on this formulation, we developed a method to compute the fluid indicator from wide-azimuth PP-AVOA data. Inversion of synthetic data corrupted with 10% random noise reliably estimates the normal and tangential fracture weaknesses and hence the fluid indicator can be determined accurately when the fractures are liquid-filled or partially saturated. As the gas saturation in the fractures increases, the quality of inversion becomes poorer. Errors of 15%–20% in g do not affect the estimation of fluid indicator significantly in case of liquid infill or partial saturation. However, for gas-saturated fractures, incorrect values of g may have a significant effect on fluid-indicator estimates.

INTRODUCTION

Studies on characterization of fractured reservoirs have considered three distinct models to represent cracks and fractures under different conditions. These include i) linear-slip model (Schoenberg, 1980; 1983; Schoenberg and Sayers, 1995), which is equivalent to thin parallel layers (Wu et al., 2005); ii) aligned, but isolated cracks (Hudson, 1980; 1981; Schoenberg and Douma, 1988); and iii) cracks hydraulically connected with pores (Thomsen, 1995; Hudson et al., 1996). Bakulin et al. (2000) demonstrated that these three models of fractures lead to the same anisotropic properties of the embedding medium. Hsu and Schoenberg (1993) introduced the dimensionless quantities normal weakness Δ_N and tangential weakness Δ_T for rotationally invariant fractures in the general linear-slip model. These weaknesses represent various conditions of fluid saturation. We further note that for fractures in presence of equant porosity, frequencies used in seismic exploration for hydrocarbon are low enough to allow squirting of fluid from cracks to the equant pores and vice versa, leading to equalization of pressure as the seismic waves propagate through the medium. This, in effect, increases the compliance of the fractures. On the contrary, incompressible fluids in isolated cracks decrease the compliance significantly. An interesting observation from these previous studies is that for weak fracture density, Δ_T does not depend on fluid saturation, whereas Δ_N is significantly affected by fluid infill.

Conventionally, P- and S-wave traveltime data are used to estimate the weak anisotropy parameters that are related to the excess fracture compliances — a combination of fracture dimension, interaction, and fluid properties (Grechka et al., 2003). Recently, there has been a growing interest to determine the fracture infill from kinematics of seismic-wave propagation in fracture-induced anisotropic media. Some studies on the characterization of the fluid saturation in fractured reservoir from observed seismic reflection traveltimes and amplitudes have shown encouraging results. From an Oman 3D experiment, van der Kolk et al. (2001) concluded that the shear-wave splitting in a reservoir containing aligned fractures is larger for gas-filled fractures than for fluid-filled fractures, in

Manuscript received by the Editor July 14, 2005; revised manuscript received November 4, 2005; published online May 24, 2006.
[1]Indian School of Mines, Department of Applied Geophysics, Dhanbad 826 004, India. E-mail: ranjitshaw@yahoo.co.in.
[2]The University of Texas at Austin, Department of Geological Sciences and Institute for Geophysics, John A. and Katherine G. Jackson School of Geosciences, 4412 Spicewood Springs Road, Austin, Texas 78759. E-mail: mrinal@ig.utexas.edu.

sharp contrast to the general belief that shear-wave splitting is independent of the nature of fluid filling the fractures. Angerer et al. (2002) observed that the asymmetry in the time delays of converted PS waves from a reservoir with horizontal interfaces is sensitive to the fluid infill if the fractures are oblique. Grechka and Tsvankin (2004) indicated that for oblique fractures, the shear-wave splitting parameter becomes dependent on the fracture infill. Reservoir characterization using kinematic attributes, such as azimuthal variation in normal moveout (NMO) velocity or traveltime, requires a substantial reservoir thickness for the observed effects to become appreciable. On the other hand, local variation in physical properties of the rocks around an interface separating two different media yield observable amplitude attributes such as AVO and AVOA. The potential for using AVOA data to determine fracture orientation and fracture density has been well established from both a theoretical point of view (Rüger and Tsvankin, 1997; Rüger, 1998; Zhu et al., 2004; Chen et al., 2005) and application to field data (Lynn et al., 1999; Gray and Head, 2000; Hall et al., 2002). Several workers investigated the effects of fluid infill on AVOA (Sayers and Rickett, 1997; MacBeth, 1999; Shen et al., 2002). However, AVOA data have not been extensively used to characterize the fracture infill quantitatively. Liu et al. (2001) showed that P- and converted S-wave AVO analysis can discriminate pore fluids in a fractured reservoir. In the present work, we show that PP-AVOA data can be directly inverted for fluid content in the fractures. To achieve this objective, we express the approximate (linearized) PP- and PS-reflection coefficients in terms of the fracture weaknesses instead of Thomsen parameters. We use a Born formalism (Shaw and Sen, 2004) to derive the sensitivity of AVOA to fracture weaknesses. We show that if the fracture weaknesses are small, inversion of PP-AVOA data yields reliable estimates of the (fracture) weaknesses of a medium with a set of rotationally invariant vertical fractures. Our results also show that PP-AVOA is insensitive to the microcorrugation/roughness on the fracture plane with ridges and troughs parallel to fracture strike, whereas the PS-AVOA contains this important information on the fracture microstructure.

The basic requirement for AVOA analysis is true-amplitude 3D data with wide azimuthal coverage (Williams and Jenner, 2002). When the azimuth-offset distribution is sparse, a common practice is to stack amplitude data into azimuth sectors. Jenner (2002) emphasized the importance of accounting for NMO velocity in estimating the correct azimuthal AVO response in such cases. Angerer (2003) developed a workflow to isolate the azimuth-dependent anisotropic signal from the macro-binned and azimuth-sectored seismic amplitudes observed over wide azimuths. Luo and Evans (2004) put forward a strong argument for using multiazimuth AVO instead of narrow-azimuth data for reliable fracture mapping. Shen et al. (2002) observed that the effects of the elastic properties of the background rocks often mask the AVO responses from fractures. Thus, meaningful fracture characterization using AVOA requires isolation of the contribution from the fractures to the observed amplitudes.

In this paper, we propose a method that uses full-azimuth AVO data. We assume that the orientation of the vertical fractures and the physical parameters of the unfractured background rocks have been determined from conventional methods, *e.g*, well log data, NMO velocity, or conventional AVO analysis. Our numerical experiments on noise-corrupted synthetic AVOA data for different cases of fluid-saturated, vertical fractures, viz. gas-, partial-, and brine-filled, embedded in an isotropic host medium show that both the normal and the tangential fracture weaknesses can be estimated reliably. Because g, the square of ratio of S- to P-wave velocity in the host medium, is a priori information in our procedure, we investigated the effects of error in the assumed value of this ratio. The results show that 15–20% errors in g do not affect the estimate of fluid indicator significantly when the fractures are fully or partially saturated with liquid. However, the same is not true for dry or gas-saturated fractures.

THEORY

We follow Grechka et al. (2003) to express the stress-displacement relationship across a set of equi-spaced, parallel, vertical fractures represented by general slip (Schoenberg and Sayers, 1995). Assuming that the traction $\boldsymbol{\sigma}$ across the fracture plane is continuous, the discontinuity of the slip vector is

$$\mathbf{u} = \mathrm{h}\mathbf{K}\boldsymbol{\sigma}, \tag{1}$$

where h denotes fracture separation. The excess compliance matrix $\mathbf{K}$ has the form

$$\mathbf{K} = \begin{bmatrix} \mathrm{K_N} & \mathrm{K_{NH}} & \mathrm{K_{NV}} \\ \mathrm{K_{NH}} & \mathrm{K_H} & \mathrm{K_{VH}} \\ \mathrm{K_{NV}} & \mathrm{K_{VH}} & \mathrm{K_V} \end{bmatrix}. \tag{2}$$

The notation of the components of $\mathbf{K}$ indicates the meaning of the excess compliances (Bakulin et al., 2000). For example, $\mathrm{K_N}$ is the ratio of discontinuity in displacement component $[\mathrm{u_1}]$ normal to the fracture plane to the normal stress σ_{11} per unit spacing of the fractures. Similarly, the tangential compliances $\mathrm{K_H}$ and $\mathrm{K_V}$ are related to the shear stresses σ_{12} and σ_{13}, respectively. The off-diagonal compliance elements represent cross-coupling between normal displacement and shear stress, or the tangential component of displacement and normal stress. $\mathrm{K_{NV}}$ represents the coupling between $[\mathrm{u_1}]$ and σ_{13}, or between $[\mathrm{u_3}]$ and σ_{11}. Nonvanishing $\mathrm{K_{NV}}$ implies that the normal and shear slips are coupled, which may arise from microcorrugation or roughness of fracture surfaces. For fractures with compliances that are invariant under rotation about an axis normal to the fracture plane, $\mathrm{K_{NV}} = \mathrm{K_{NH}} = \mathrm{K_{VH}} = 0$, and $\mathrm{K_V} = \mathrm{K_H} = \mathrm{K_T}$. The ratio of the normal to the tangential excess compliance $\mathrm{K_N/K_T}$ is an indicator of the fluid content (Schoenberg and Sayers, 1995). This factor tends to zero for fluid-saturated fractures ($\mathrm{K_N} \approx 0$) and is nearly a unity if the fractures are dry or gas-saturated ($\mathrm{K_N} \approx \mathrm{K_T}$).

We consider a homogeneous isotropic medium with Lame's parameters λ and μ in which are embedded a set of parallel, vertical fractures adequately represented by general slips (equation 1). Because of the presence of the fractures, the stiffness matrix is modified as follows (Schoenberg and Sayers, 1995; Sayers and Rickett, 1997):

$$\mathbf{C} = (\lambda + 2\mu)[\mathbf{C}^{\mathrm{b}} - \mathbf{C}^{\mathrm{f}}], \tag{3}$$

with

$$\mathbf{C}^{b} = \begin{bmatrix} 1 & \chi & \chi & 0 & 0 & 0 \\ & 1 & \chi & 0 & 0 & 0 \\ & & 1 & 0 & 0 & 0 \\ & & & g & 0 & 0 \\ & & & & g & 0 \\ & & & & & g \end{bmatrix} \text{ and}$$

$$\mathbf{C}^{f} = \begin{bmatrix} \Delta_N & \chi\Delta_N & \chi\Delta_N & 0 & \sqrt{g}\Delta_{NV} & \sqrt{g}\Delta_{NH} \\ & \chi^2\Delta_N & \chi^2\Delta_N & 0 & \chi\sqrt{g}\Delta_{NV} & \chi\sqrt{g}\Delta_{NH} \\ & & \chi^2\Delta_N & 0 & \chi\sqrt{g}\Delta_{NV} & \chi\sqrt{g}\Delta_{NH} \\ & & & 0 & 0 & 0 \\ & & & & g\Delta_V & g\sqrt{g}\Delta_{VH} \\ & & & & & g\Delta_H \end{bmatrix},$$

where $g = \mu/(\lambda + 2\mu)$ is the square of the ratio of S-wave velocity β and P-wave velocity α in the background medium, $X = \lambda/(\lambda + 2\mu) = 1 - 2g$, and the fracture weaknesses are

$$\Delta_N = \frac{(\lambda + 2\mu)K_N}{1 + (\lambda + 2\mu)K_N} \quad \Delta_{NV} = \frac{\sqrt{\mu(\lambda + 2\mu)}K_{NV}}{1 + \sqrt{\mu(\lambda + 2\mu)}K_{NV}}$$

$$\Delta_V = \frac{\mu K_V}{1 + \mu K_V} \quad \Delta_{NH} = \frac{\sqrt{\mu(\lambda + 2\mu)}K_{NH}}{1 + \sqrt{\mu(\lambda + 2\mu)}K_{NH}}$$

$$\Delta_H = \frac{\mu K_H}{1 + \mu K_H} \quad \Delta_{VH} = \frac{\sqrt{\mu(\lambda + 2\mu)}K_{VH}}{1 + \sqrt{\mu(\lambda + 2\mu)}K_{VH}}. \quad (4)$$

As observed earlier, for a set of fractures with properties that are invariant under rotation about the normal to the fracture faces, $\Delta_V = \Delta_H = \Delta_T$, say. Further, if the medium has a very small fracture density, the factor Δ_N/Δ_V varies proportionally to K_N/K_V (Table 1) and is a fluid indicator.

In general, the stiffness of the fractured medium given by equation 3 represents a monoclinic medium. Assuming that the fractures can be represented by planar discontinuities with no corrugation or surface roughness, the medium becomes transversely isotropic with a horizontal axis of symmetry (HTI). The AVOA over such media has been investigated extensively (Mallick and Frazer, 1991; Rüger, 1997; 1998; Rüger and Tsvankin, 1997). Conventionally, the anisotropy of such media is represented by weak anisotropy parameters (Thomsen, 1986) that have a simple relationship to the fracture weaknesses (Bakulin et al., 2000). Here, we express the reflection coefficient directly as a function of the fracture weakness:

$$R^{obs}(\theta, \phi) = R^{iso}(\theta) + R^{ani}(\theta, \phi; \Delta), \quad (5)$$

where θ is the angle of incidence, ϕ is the azimuth of the seismic line with respect to the symmetry axis of the fracture system, and Δ represents the vector of fracture weakness given by

$$\boldsymbol{\Delta}^T = (\Delta_N, \Delta_V, \Delta_H, \Delta_{NV}, \Delta_{NH}, \Delta_{VH}). \quad (6)$$

$R^{iso}(\theta)$ and $R^{ani}(\theta, \phi; \Delta)$ represent the isotropic and anisotropic parts of the reflection coefficient, respectively. To linearize the reflection coefficients, we represented in an earlier work (Shaw and Sen, 2004) a weak anisotropic medium as a volume of scatterers embedded in a background isotropic medium. We used asymptotic ray theory and the method of stationary phase to show that the scattering function $S(\mathbf{r}_o)$ corresponding to the singly scattered wavefield relates to the linearized PP-reflection coefficient as

$$R_{PP}(\theta) = \frac{1}{4\rho_o \cos^2\theta} S(\mathbf{r_o}), \quad (7)$$

with

$$S(\mathbf{r_o}) = \Delta\rho\xi + \Delta c_{ijkl}\eta_{ijkl}, \quad (8)$$

$$\xi = t_i t_i'|_{\mathbf{r}=\mathbf{r_o}}, \quad (9)$$

$$\eta_{ijkl} = t_i' p_j' t_k p_l|_{\mathbf{r}=\mathbf{r_o}}, \quad (10)$$

where ρ_o is the density of the background medium and $\Delta\rho$ and Δc_{ijkl} represent the perturbation in density and elastic stiffness, respectively. $\mathbf{p}$ and $\mathbf{t}$ are the slowness and the polarization vectors, respectively. The prime denotes the scattered wave. The position vector $\mathbf{r}_o$ is the point on a horizontal interface separating two weak

Table 1. Relation of fracture weaknesses with microfracture properties in commonly used models for natural fractures in hydrocarbon reservoirs; e represents the fracture density.

Fracture parameter	Linear-slip model, (Schoenberg and Sayers, 1995)	Thin, penny-shaped, aligned cracks (Hudson, 1980)		Aligned cracks in medium with equant porosity (Thomsen, 1995)	
		Dry/gas-filled	Liquid-filled	Dry/gas-filled	Liquid-filled
Normal weakness, ΔN	$\frac{(\lambda + 2\mu)K_N}{1 + (\lambda + 2\mu)K_N}$	$\frac{4e}{3g(1-g)}$	≈ 0	$\frac{4e}{3g(1-g)}$	$q\frac{4e}{3g(1-g)}$
Tangential weakness, ΔT	$\frac{\mu K_T}{1 + \mu K_T}$			$\frac{16e}{3(3-2g)}$	
Fluid indicator $\approx g\frac{\Delta_N}{\Delta_T}$	$\frac{K_N}{K_T}$	$\frac{7}{8}\left(1 + \frac{5s}{2\pi f}\right)^{-1}$		$q\frac{3-2g}{4(1-g)}$	

(an)isotropic media, where Snell's law of reflection for a source-receiver pair is satisfied. Summation convention applies to equations 8 and 9. Comparing equations 3, 7, and 8 shows that the dependence of the PP-reflection coefficients on fracture weaknesses can be derived by collecting the coefficients η_{ijkl} corresponding to each weakness and simplifying the expression in the desired form of incidence angle and azimuth (Appendix A). No approximations, other than dilute fracture distribution and weak fracture compliances (Δ_N, etc $\ll 1$) are required for the validity of equation 3.

If information on the isotropic medium in which the fractures are embedded is known a priori, or estimated by established methods, equation 5 can be written, under the assumption of weak fracture weakness, as

$$\delta\mathbf{R} = \mathbf{R}_{PP}^{obs}(i,\theta) - \mathbf{R}_{PP}^{iso}(\theta) = \mathbf{A}\boldsymbol{\Delta}, \tag{11}$$

where the sensitivity matrix $\mathbf{A}$ is given by

$$\mathbf{A} = \frac{1}{4}[a_N,\ a_V,\ a_H,\ a_{NV},\ a_{NH},\ a_{VH}], \tag{12}$$

and for a given incidence angle and azimuth, the row elements of $\mathbf{A}$ are given by

$$\begin{aligned}
a_N &= (1-2g)^2 + [(1-2g) + 2g(1-2g)\cos 2\phi]\sin^2\theta \\
&\quad + \left[\left(1 - 2g + \frac{3}{2}g^2\right) + 2g(1-g)\cos 2\phi \right. \\
&\quad \left. + \frac{1}{2}g^2\cos 4\phi\right]\sin^2\theta\tan^2\theta \\
a_V &= -2g(1+\cos 2\phi)\sin^2\theta \\
a_H &= \frac{g}{2}(1-\cos 4\phi)\sin^2\theta\tan^2\theta \\
a_{NV} &= 0 \\
a_{NH} &= 2\sqrt{g}(1-g)\sin 2\phi\sin^2\theta + \sqrt{g}[2(1-g)\sin 2\phi \\
&\quad + g\sin 4\phi]\sin^2\theta\tan^2\theta \\
a_{VH} &= 0.
\end{aligned} \tag{13}$$

The linearized PP-reflection coefficients are insensitive to the microcorrugation or roughness in the fracture surface, because $a_{NV} = 0$. For rotationally invariant fractures, substituting equation 13 into 11 and rearranging the terms results in an expression for linearized plane-wave PP-reflection coefficient in the form of equation 1 of Rüger and Tsvankin (1997), which has been extensively used for azimuthal AVO analysis. We further observed that the difference of the P-wave reflection coefficient along and perpendicular to the fracture symmetry axes is

$$\begin{aligned}
\Delta\mathbf{R}(\theta) &= \mathbf{R}_{PP}^{obs}(\theta,\phi=0^\circ) - \mathbf{R}_{PP}^{obs}(\theta,\phi=90^\circ) \\
&= g[\{(1-2g)\Delta_N - \Delta_T\}\sin^2\theta \\
&\quad + (1-g)\Delta_N\sin^2\theta\tan^2\theta],
\end{aligned} \tag{14}$$

which reduces to equation 16 of Sayers and Rickett (1997), for normalized excess compliances $(\lambda + 2\mu)K_N$ and μK_T much smaller than unity.

The following differences exist between our work and that of Sayers and Rickett (1997). We obtained expressions for both PP and mode-converted (PS) linearized plane-wave reflection coefficients in terms of fracture weaknesses. To accomplish this, we used a general-slip model to express the elastic coefficients of the fractured medium in terms of fracture weaknesses and scattering theory (Shaw and Sen, 2004) to linearize the reflection coefficient. On the other hand, Sayers and Rickett (1997) defined the Thomsen parameters in terms of the fracture compliances normalized with respect to the isotropic background-rock elastic parameters, and substituted these values in the expressions for linearized PP-reflection coefficients only over HTI media (Rüger, 1998). These two expressions are equivalent for a fractured medium with rotationally invariant fractures. However, because our representation of fractures is more general, the effects of microcorrugation on PP- and PS-AVOA become apparent.

For mode-converted waves (PS), an equation equivalent to equation 11 can be written as

$$\delta\mathbf{R}_{PS} = \mathbf{R}_{PS}^{obs}(\theta,\phi) - \mathbf{R}_{PS}^{iso}(\theta) = \mathbf{B}\boldsymbol{\Delta}, \tag{15}$$

where the sensitivity matrix $\mathbf{B}$ is given by

$$\mathbf{B} = \frac{\sin\theta}{2\sqrt{g}\cos\zeta\sin(\theta+\zeta)}[b_N, b_V, b_H, b_{NV}, b_{NH}, b_{VH}], \tag{16}$$

with

$$\begin{aligned}
b_N &= g(1-2g)(1+\cos 2\phi)\sin\zeta\cos\zeta + \frac{1}{2}g^2(3 \\
&\quad + 4\cos 2\phi + \cos 4\phi)\sin^2\theta\sin\zeta\cos\zeta \\
b_V &= -\frac{g}{2}(1+\cos 2\phi)\sin 2\theta\cos 2\zeta \\
b_H &= \frac{g}{2}(1-\cos 4\phi)\sin^2\theta\sin\zeta\cos\zeta \\
b_{NV} &= \sqrt{g}\cos\phi[\{(1-g) + g\cos 2\phi\}\sin\theta\sin(2\zeta-\theta) \\
&\quad - (1-2g)\cos\theta\cos(2\zeta-\theta)] \\
b_{NH} &= \sqrt{g}\sin 2\phi[(1-2g)\sin\zeta\cos\zeta \\
&\quad + 2g(1+\cos 2\phi)\sin^2\theta\sin\zeta\cos\zeta] \\
b_{VH} &= g\sqrt{g}\sin 2\phi\sin\theta\sin(2\zeta-\tau).
\end{aligned} \tag{17}$$

Here, $\tan\tau = \tan\theta\cot\phi$, and ζ represents the angle of reflection for the converted SV wave.

Because, in general, b_{NV} is not zero, the linearized PS-reflection coefficient (equation 17) is sensitive to the 2D microcorrugation or roughness in the fracture surfaces with ridges and troughs parallel to the fracture strike direction.

RESULTS

We first investigated how the incompressibility of the fluid filling cracks affects the fluid indicator in a fractured reservoir with isolated, penny-shaped cracks or with cracks hydraulically connected to equant pores. The expressions for the normal weakness, the tangential weakness, and the fluid indicator are summarized in Table 1.

In the linear-slip model for fractures, the fluid indicator is given by Schoenberg and Sayers (1995) as

$$\text{fluid indicator} = \frac{K_N}{K_T} \approx g\frac{\Delta_N}{\Delta_T}. \tag{18}$$

For aligned, penny-shaped cracks, the expression for the fluid indicator simplifies to (Hudson, 1980)

$$\text{fluid indicator} = \frac{7}{8}\left[1 + \frac{5\varsigma}{2\pi f}\right]^{-1}, \tag{19}$$

where f is the aspect ratio of the cracks, i.e., the ratio of the crack aperture to crack diameter, and $\varsigma = \kappa'/\kappa$ with κ and κ' representing the incompressibility of the rock matrix and the inclusion fluid, respectively.

For fractures that are hydraulically connected to equant pores, we follow Thomsen (1995) and Bakulin et al. (2000) to write the expression for fluid indicator as

$$\text{fluid indicator} = q\frac{3 - 2g}{4(1 - g)}, \tag{20}$$

where

$$q = \frac{1 - \varsigma}{1 - \varsigma\{1 - (A_p\bar{\phi}_p + A_c\bar{\phi}_c)\}}. \tag{21}$$

Here, $\bar{\phi}_p$ and $\bar{\phi}_c$ represent the fractional primary (equant) porosity and the crack porosity, respectively. Although both the coefficients $A_p = (3 - 2g)/2g$ and $A_c = (2 - 3g)/3\pi f(1 - g)$ depend on the background-medium properties, the latter depends, additionally, on the fracture-aspect ratio. Note that Bakulin et al. (2000) identified the factor q as the fluid indicator, which is simply the fluid influence factor of Thomsen (1995) scaled by $(1 - \varsigma)$, under the low-frequency approximation. For gas-saturated fractures, $\kappa' \approx 0$, implying $q \approx 1$ from equation 21. Under this condition, equation 20 reduces to

$$\text{fluid indicator} = 1 - \frac{\nu}{2}, \tag{22}$$

where ν is the Poisson's ratio of the background medium. Equation 22 is a very simple and well-known result (Bakulin et al., 2000) that has far-reaching implications for estimating fluid content.

It is generally believed that the interaction of fractures with equant pores decreases the fluid indicator. In other words, if fractures are dry or gas-saturated, but are isolated, the fluid indicator approaches unity. On the other hand, the same set of fractures with the same state of fluid saturation behaves as though partially filled when the fractures and equant pores in the host medium are hydraulically connected. To understand the interplay of the roles of fluid, matrix, and fracture geometry, we designed a numerical experiment based on a set of aligned, penny-shaped cracks with crack density 0.05 and aspect ratio 0.01 embedded in an isotropic chalk with P- and S-wave velocities 3620 m/s and 1810 m/s, respectively. We computed the fluid indicator using equation 20 for values of ς, the ratio of the incompressibility of the fluid infill and rock matrix between 0 (dry/gas) and 0.3, for fractional crack porosity varying between 0 (no cracks, all equant pores) to 1 (all cracks, no equant pores) at an interval of 0.2. The solid lines in Figure 1 depict the variation of fluid indicator with ς, which shows that the fluid indicator increases, for a specific case of crack-pore interaction, as the fluid becomes more and more compressible. On the other hand, for any fixed value of ς, an increase in crack porosity decreases the fluid indicator, because of fluid flow between the cracks and pores.

Next, we selected four sets of isolated cracks with aspect ratios, 0.1, 0.8, 0.5, and 0.3, and computed the fluid indicator from equation 19 for the same range of ς. These results are depicted in Figure 1. The fluid indicator computed from equations 19 and 20 are nearly the same over the entire range of selected ς for appropriate combinations of fracture-aspect ratio and fractional porosity, indicating that the fluid indicator depends on a complex combination of microstructural properties of fractures and the elastic properties of the solid matrix and the fluid infill. However, if the fractures are dry or gas-saturated, the value of the fluid indicator approaches unity whether or not the fractures interact with pores. From these results, it appears that characterizing gas-saturated fractures should be easy and unambiguous. We discuss the practical difficulties in estimating the fluid indicator in gas-saturated fractures in the following section.

To understand how the normal and fracture weaknesses affect the PP-reflection coefficients at different incidence angles and azimuths, we selected an isotropic host medium with P-wave velocity α equal to twice the S-wave velocity β, corresponding to g = 0.25, common for sedimentary rocks. We used equation 13 to compute the coefficients a_N and $a_T = a_V + a_H$ for incidence angles varying between 0° and 40° at intervals of 2° and for azimuths varying between 0° and 90° at intervals of 5°. The results (Figure

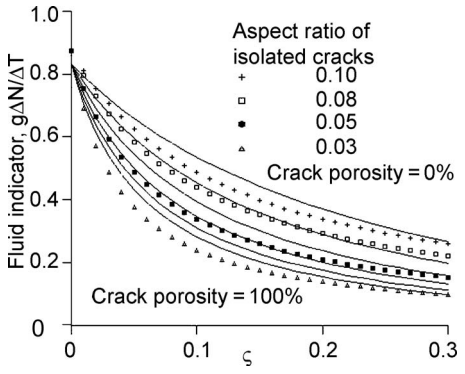

Figure 1. Variation of fluid indicator with the ratio of incompressibilty of fluid and solid matrix. Solid lines refer to fractures hydraulically connected to equant pores with fractional crack porosity shown at an interval of 20% computed by using equation 20. The discrete symbols refer to aligned, but isolated, penny-shaped cracks with aspect ratio indicated in the legend.

2) show that the PP-reflection coefficients have greater sensitivity to Δ_N than Δ_T. Note that the reflection coefficients along the fracture strike direction (azimuth = 90°) are independent of the tangential weakness. Further, Δ_N affects the reflection coefficients at most incidence angles. On the other hand, the effect of Δ_T on PP-reflection coefficients is prominent at large angles of incidence only — a behavior similar to the effect of S-wave velocity on the PP-reflection coefficient from an interface separating two isotropic media. The reason can be found in the structure of equation 3, which shows that the tangential weakness Δ_T of the fractures modifies the shear modulus of the background isotropic medium only, and does not affect the P-wave velocity in the unfractured medium.

To determine the accuracy of the linearized reflection coefficients expressed in terms of normal and tangential fracture weaknesses, we considered a set of rotationally invariant vertical fractures with normal and tangential weaknesses 0.20 and 0.05, respectively, embedded in an isotropic chalk (Shen et al., 2002) characterized by P-wave velocity, S-wave velocity, and density of 3620 m/s, 1810 m/s, and 2420 kg/m^3, respectively. We further assumed that the fracture density is so weak that the density of the fractured chalk is the same as that of the isotropic chalk in which the fractures are embedded. We used equation 3 to compute the elastic coefficients of the fractured medium and the reflectivity method (Fryer and Frazer, 1984) to compute the exact PP-reflection coefficients from an interface separating the fractured medium from the isotropic background. We considered a range of incidence angles 0–40° and azimuths 0–90° for this purpose. We also computed the linearized PP-reflection coefficients from equation 7 for the same range of incidence angles and azimuths. Figure 3 compares the exact and the linerarized PP-reflection coefficients.

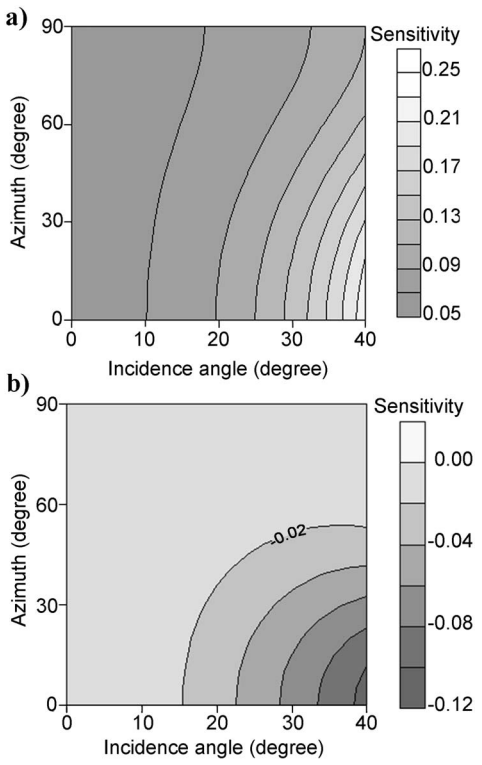

Figure 2. Dependence of linearized PP-reflection coefficient on (a) normal weakness Δ_N and (b) tangential weakness Δ_T.

The linearized PP-reflection coefficients match the exact reflection coefficients over a wide range of incidence angles and azimuths. The discrepancies between the two are largest for incidence angles exceeding 30°, but are limited to 5–6% for this example.

Estimation of fluid indicator

Because our method requires the knowledge of the orientation of the vertical fractures as well as information about the physical parameters of the overlying and unfractured background rocks, we assume that these parameters have been determined from conventional methods, *e.g.*, well log data, NMO velocity, or conventional AVO analysis. To estimate the fluid indicator, we first compute the exact reflection coefficient $\mathbf{R}_{PP}^{bgd}(\theta)$ for the interface separating the overlying medium from the isotropic medium in which fractures are embedded, and subtract this from the observed amplitude data

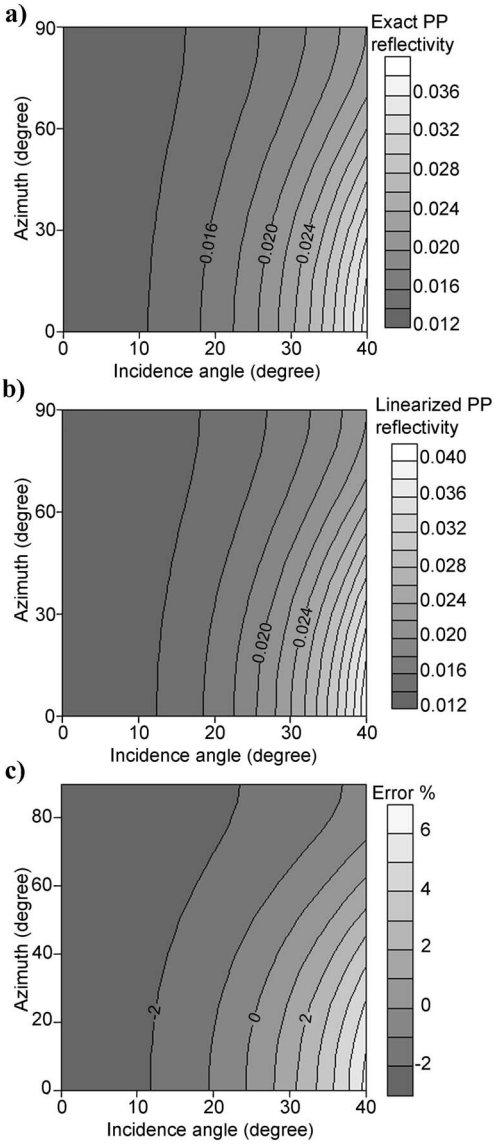

Figure 3. Variation of reflection coefficients with angles of incidence and azimuth: (a) exact reflection coefficients, (b) linearized reflection coefficients, and (c) difference between linearized and exact reflection coefficients.

to isolate the effects of fractures on the AVOA. These data, $\delta\mathbf{R} = \mathbf{R}_{PP}^{obs}(\theta,\phi) - \mathbf{R}_{PP}^{bgd}(\theta)$, form the input to a linear least-squares inversion to estimate the fracture weaknesses Δ_N and Δ_T:

$$\Delta_I = [\mathbf{A}^T\mathbf{A}]^{-1}\mathbf{A}^T\delta\mathbf{R}, \quad (23)$$

where $\Delta_I^T = [\Delta_N \Delta_T]$.

Then, we use equation 18 to estimate the fluid indicator.

We used the exact formulation to generate PP-AVOA data for an interface separating a shale from an isotropic chalk described in Table 2 for four different fluid saturations, viz. 100% gas-saturated and 10%, 30%, and 100% brine-saturated fractures. We varied the incidence angle between 0° and 40° at intervals of 5° and considered azimuths varying between 0° and 90° at intervals of 15°. Using known parameters for the background medium, we isolated the effects of the fractures on the observed PP-AVOA and added random noise (Press et al., 1989) of 10% of the maximum amplitude over the entire range of incidence angles and azimuths. We inverted these data for the fracture weaknesses Δ_N and Δ_T, and computed the fluid indicator using a priori knowledge of g of the unfractured medium. Figure 4a shows the estimated fluid indicators and their scatter for different fluid-infill models. The partial-saturation cases (brine/gas) with fluid indicators 0.248 and 0.487 correspond to fractures having aspect ratio 0.01 and fracture density 0.023, with brine saturation of 30% and 10%, respectively. The results are also tabulated in Table 3 for a quantitative appraisal. The results show that inversion of P-wave AVOA data yields satisfactory estimates of fracture weaknesses and fluid infill when the fractures are brine-filled or partially saturated. For gas-saturated fractures, the fluid indicator is underestimated.

Because there is uncertainty in g, we investigated the effect of error in g on the estimation of fluid indicator. We repeated the experiment described above for values of g varying between 0.2 and 0.3 at intervals of 0.01. For each value of g, we computed the fluid indicator and the error estimates (Figure 4b). We observed that for fractures that are partially or fully saturated with brine, an error up to 15%–20% in the value of assumed g does not affect the accuracy of fluid indicator significantly. However, for dry or gas-saturated fractures, an error in g may affect the fluid-indicator estimate to a large extent if g is underestimated.

Table 2. Parameters of an interface separating an isotropic medium from a fractured medium (after Shen et al., 2002; MacBeth, 1999).

Medium	Density, kg/m^3	α, m/s	β, m/s
Shale	2300	2460	1230
Chalk	2420	3620	1810
Brine	1100	1710	—

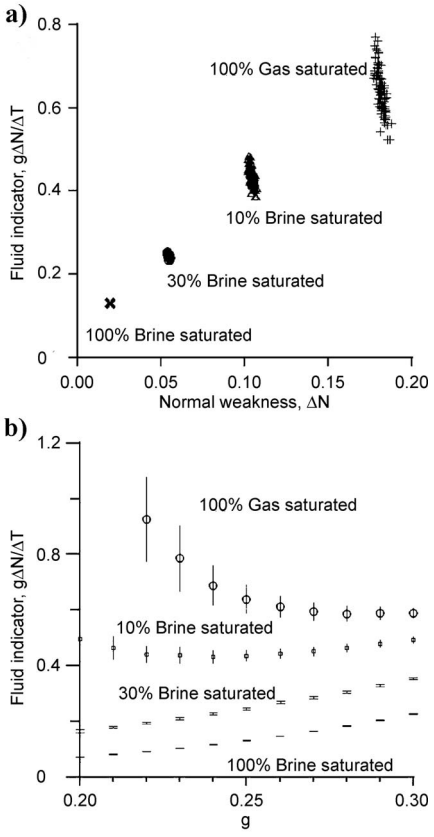

Figure 4. (a) Fluid-indicator estimates from noisy synthetic AVOA data for different conditions of fluid saturation, and (b) the effect of error in g on the fluid indicator.

CONCLUSIONS

Because previous studies showed an equivalence in the elastic properties of commonly used models, we selected the linear-slip theory to represent the macroproperties of the fractures. To quantitatively estimate the fluid content in a vertically fractured reservoir, we selected the ratio of the normal weakness to the tangential weakness of the incipient fractures, defined by linear-slip theory as a measure of the fluid indicator. We showed that for a wide range of the ratio of incompressibility of the fluid infill to the background solid matrix, the two models, viz. (i) isolated cracks and (ii) cracks in-

Table 3. Inversion of PP-AVOA data to estimate fracture weakness and fluid indicator.

Brine/gas saturation	Normal weakness, Δ_N		Tangential weakness, Δ_T		Fluid indicator = $g\Delta_N/\Delta_T$	
	True	Estimated	True	Estimated	True	Estimated
100% gas-saturated	0.178	0.181 ± 0.002	0.053	0.071 ± 0.006	0.840	0.640 ± 0.053
10% brine-saturated	0.103	0.104 ± 0.001	0.053	0.060 ± 0.003	0.487	0.436 ± 0.021
30% brine-saturated	0.054	0.054 ± 0.001	0.053	0.055 ± 0.001	0.248	0.245 ± 0.005
100% brine-saturated	0.021	0.019 ± 0.001	0.053	0.037 ± 0.001	0.099	0.131 ± 0.001

teracting with pores, are practically indistinguishable. From this, we conclude that interpretation of a fluid indicator would lead to ambiguity in models of crack porosity.

We investigated the sensitivity of the linearized PP- and PS-reflection coefficients to the normal and tangential weaknesses. We represented the elastic properties of a set of vertical, parallel fractures embedded in an otherwise isotropic medium by general slips. The simple relationship of the linearized reflection coefficients from a weak anisotropic media to the singly scattered wavefield allowed us to derive expressions for the sensitivity of PP- and PS — reflection coefficients to fracture weakness. We observed that the PP-AVOA does not contain information on the weakness Δ_{NV} that defines 2D microcorrugation or fracture roughness with ridges and valleys parallel to the fracture strike direction. On the other hand, PS-AVOA is sensitive to this parameter. Furthermore, the tangential weakness does not contribute to either the PP — or the PS-reflection coefficients along the direction of the fracture strike. Our method for estimating fluid indicator uses full-azimuth AVO data from which the contributions of the fractures have been isolated. Least-squares inversion of synthetic data corrupted with 10% random noise for different cases of fluid saturation in the fractures shows that the estimated fluid indicators agree reasonably with the assumed values. For dry or gas-saturated fractures, there is a systematic over-estimation of the tangential weakness that results in an underestimate of the fluid indicator. We conclude that errors up to 20% in g for the unfractured host medium, which is a priori in our method, do not affect the fluid-indicator estimate significantly if the fractures are fluid-filled or partially saturated. As the gas saturation of the fracture increases, inaccuracy in g affects the fluid-indicator estimate significantly.

ACKNOWLEDGMENTS

RKS acknowledges the financial support from the Department of Science and Technology, New Delhi under grant no. ESS/16/203/2004. Suggestions made by the associate editor and three anonymous reviewers have improved the manuscript considerably.

APPENDIX A

SENSITIVITY OF LINEARIZED REFLECTION COEFFICIENTS TO FRACTURE WEAKNESS

To derive the expressions for sensitivity of linearized PP and PS-reflection coefficients to the fracture weaknesses, we rewrite the second term in the right hand side of equation 8 as $\Sigma_{I=1}^{6}\Sigma_{J=1}^{6}C'_{IJ}E_{IJ}$, where the elements of the two 6×6 matrices C' and E' are given by

$$C'_{IJ} = \Delta c_{ijkl} \tag{A-1}$$

and

$$E'_{IJ} = \eta_{ijkl} \tag{A-2}$$

with

$$I = i\delta_{ij} + (9 - i - j)(1 - \delta_{ij}) \tag{A-3}$$

and

$$J = k\delta_{kl} + (9 - k - l)(1 - \delta_{kl}). \tag{A-4}$$

δ_{ij} and δ_{kl} are Kronecker delta.

We explain the procedure through an example. From equations 3, 4, 7, 8, and A-2, the sensitivity of the normal weakness of the fractures to the linearized PP-reflection coefficients is given by

$$\frac{\lambda + 2\mu}{4\rho_o \cos^2\theta}[E'_{11} + \chi(E'_{12} + E'_{21} + E'_{13} + E'_{31}) + \chi^2(E'_{22} + E'_{33} + E'_{23} + E'_{32})]. \tag{A-5}$$

The polarization vectors corresponding to the incident and the reflected waves are given by

$$t = [\sin\theta\cos\phi, \sin\theta\sin\phi, \cos\theta] \tag{A-6}$$

and

$$t' = [-\sin\theta\cos\phi, -\sin\theta\sin\phi, \cos\theta], \tag{A-7}$$

respectively. Similarly, the corresponding slowness vectors are

$$p = \frac{1}{\alpha}[\sin\theta\cos\phi, \sin\theta\sin\phi, \cos\theta] \tag{A-8}$$

and

$$p' = \frac{1}{\alpha}[-\sin\theta\cos\phi, -\sin\theta\sin\phi, \cos\theta]. \tag{A-9}$$

Thus,

$$E'_{21} = \eta_{2211} = t'_2 p'_2 t_1 p_1|_{r=r_o} = \frac{1}{\alpha^2}\sin^4\theta\sin^2\phi\cos^2\phi. \tag{A-10}$$

In a similar way, we write the expressions for E'_{IJ} corresponding to PP reflections from a horizontal interface as

$$E_{11} = \sin^4\theta\cos^4\phi \quad E_{41} = -E_{14}$$

$$E_{12} = \sin^4\theta\sin^2\phi\cos^2\phi \quad E_{42} = -E_{24}$$

$$E_{13} = \sin^2\theta\cos^2\theta\cos^2\phi \quad E_{43} = -E_{34}$$

$$E_{14} = 2\sin^3\theta\cos\theta\sin\phi\cos^2\phi$$

$$E_{44} = -4\sin^2\theta\cos^2\theta\sin^2\phi$$

$$E_{15} = -2\sin^3\theta\cos\theta\cos^3\phi$$

$$E_{45} = -4\sin^2\theta\cos^2\theta\sin\phi\cos\phi$$

$$E_{16} = 2\sin^4\theta\sin\phi\cos^3\phi$$

$$E_{46} = -4\sin^3\theta\cos\theta\sin^2\phi\cos\phi$$

$$E_{21} = E_{12} \quad E_{51} = -E_{15}$$

$$E_{22} = \sin^4\theta \sin^4\phi \quad E_{52} = -E_{25}$$

$$E_{23} = \sin^2\theta \cos^2\theta \sin^2\phi$$

$$E_{53} = -E_{35}$$

$$E_{24} = -2\sin^3\theta \cos\theta \sin^3\phi$$

$$E_{54} = E_{45}$$

$$E_{25} = -2\sin^3\theta \cos\theta \sin^2\phi \cos\phi$$

$$E_{55} = -4\sin^2\theta \cos^2\theta \cos^2\phi$$

$$E_{26} = 2\sin^4\theta \sin^3\phi \cos\phi$$

$$E_{56} = 4\sin^3\theta \cos\theta \sin\phi \cos\phi$$

$$E_{31} = E_{13} \quad E_{61} = E_{16}$$

$$E_{32} = E_{23} \quad E_{62} = E_{26}$$

$$E_{33} = \cos^4\theta \quad E_{63} = E_{36}$$

$$E_{34} = 2\cos^3\theta \sin\theta \sin\phi \quad E_{64} = -E_{46}$$

$$E_{35} = -2\cos^3\theta \sin\theta \cos\phi \quad E_{65} = -E_{56}$$

$$E_{36} = 2\sin^2\theta \cos^2\theta \sin\phi \cos\phi$$

$$E_{66} = 4\sin^4\theta \sin^2\phi \cos^2\phi,$$

where

$$E'_{IJ} = \frac{E_{IJ}}{\alpha^2},\ I,J = 1, 2, \ldots, 6. \qquad \text{(A-11)}$$

For mode-converted P-SV reflection, the coefficients $E'_{IJ} = E_{IJ}/\alpha\beta$, I,J = 1, 2, …, 6 are

$$E_{11} = \sin^2\theta \sin\zeta \cos\zeta \cos^4\phi$$

$$E_{41} = -\sin^2\theta \cos 2\zeta \sin\phi \cos^2\phi$$

$$E_{12} = \sin^2\theta \sin\zeta \cos\zeta \sin^2\phi \cos^2\phi$$

$$E_{42} = -\sin^2\theta \cos 2\zeta \sin^3\phi$$

$$E_{13} = \cos^2\theta \sin\zeta \cos\zeta \cos^2\phi \quad E_{43} = -\cos^2\theta \cos 2\zeta \sin\phi$$

$$E_{14} = \sin\theta \cos\theta \sin 2\zeta \sin\phi \cos^2\phi$$

$$E_{44} = -\sin 2\theta \cos 2\zeta \sin^2\phi$$

$$E_{15} = \sin\theta \cos\theta \sin 2\zeta \cos^3\phi$$

$$E_{45} = -\sin 2\theta \cos 2\zeta \sin\phi \cos\phi$$

$$E_{16} = \sin^2\theta \sin 2\zeta \sin\phi \cos^3\phi$$

$$E_{46} = -2\sin^2\theta \cos 2\zeta \sin^2\phi \cos\phi$$

$$E_{21} = E_{12} \quad E_{51} = -\sin^2\theta \cos 2\zeta \cos^3\phi$$

$$E_{22} = \sin^2\theta \sin\zeta \cos\zeta \sin^4\phi$$

$$E_{52} = -\sin^2\theta \cos 2\zeta \sin^2\phi \cos\phi$$

$$E_{23} = \cos^2\theta \sin\zeta \cos\zeta \sin^2\phi \quad E_{53} = -\cos^2\theta \cos 2\zeta \cos\phi$$

$$E_{24} = \sin\theta \cos\theta \sin 2\zeta \sin^3\phi \quad E_{54} = E_{45}$$

$$E_{25} = \sin\theta \cos\theta \sin 2\zeta \sin^2\phi \cos\phi$$

$$E_{55} = -\sin 2\theta \cos 2\zeta \cos^2\phi$$

$$E_{26} = \sin^2\theta \sin 2\zeta \sin^3\phi \cos\phi$$

$$E_{56} = -2\sin^2\theta \cos 2\zeta \sin\phi \cos^2\phi$$

$$E_{31} = -\sin^2\theta \sin\zeta \cos\zeta \cos^2\phi \quad E_{61} = E_{16}$$

$$E_{32} = -\sin^2\theta \sin\zeta \cos\zeta \sin^2\phi \quad E_{62} = E_{26}$$

$$E_{33} = -\cos^2\theta \sin\zeta \cos\zeta \quad E_{63} = \cos^2\theta \sin 2\zeta \sin\phi \cos\phi$$

$$E_{34} = -\sin\theta \cos\theta \sin 2\zeta \sin\phi$$

$$E_{64} = \sin 2\theta \sin 2\zeta \sin\phi \cos^2\phi$$

$$E_{35} = -\sin\theta \cos\theta \sin 2\zeta \cos\phi$$

$$E_{65} = \sin 2\theta \sin 2\zeta \sin^2\phi \cos\phi$$

$$E_{36} = -\sin^2\theta \sin 2\zeta \sin\phi \cos\phi$$

$$E_{66} = 2\sin^2\theta \sin 2\zeta \sin^2\phi \cos^2\phi.$$

APPENDIX B

NOTATIONS

Symbol(s)	Description
$\mathbf{u}$	= Displacement discontinuity vector across a fracture plane, also called slip vector
u_1, u_2, u_3	= Components of the slip along 1, 2, and 3 directions
h	= Separation between two fractures
$\mathbf{K}$	= Compliance matrix
K_N, K_V, K_H … etc	= Elements of excess compliance matrix
$\boldsymbol{\sigma}$	= Traction acting on the fracture plane
$\sigma_{12}, \sigma_{13}, \sigma_{23}$	= Elements of stress tensor
λ, μ	= Lame's parameters
$\mathbf{C}, \mathbf{C}^b, \mathbf{C}^f$	= Elastic stiffness matrices of fractured medium, background, and fractures, respectively
g	= Square of the ratio of S- and P-wave velocities in the background medium
χ	= 1 − 2g
$\boldsymbol{\Delta}, \boldsymbol{\Delta}_1$	= Fracture weakness vectors
$\Delta_N, \Delta_V, \Delta_H$ etc.	= Elements of $\boldsymbol{\Delta}$
$R(\theta,\phi)$	= Reflection coefficient at incidence angle θ and azimuth ϕ
$R_{PP}^{iso}, R_{PP}^{ani}, R_{PP}^{bgd}$	= PP-reflection coefficients
R_{PS}^{iso}	= PS-reflection coefficients
$\partial R, \Delta R$	= Difference of reflection coefficients between two cases/two azimuths
S(.)	= Scattering function
$\mathbf{r}$	= Position vector of an arbitrary point
$\mathbf{r}_o$	= Position vector of a specific point

ρ_o = Density of background medium
$\Delta\rho$ = Perturbation in density
ΔC = Perturbations in elastic stiffness parameters
$\mathbf{t}$ = Polarization vector
$\mathbf{p}$ = Slowness vector
ξ = Factor showing dependence of scattering function on density perturbation
η, E, E′ = Factors showing dependence of scattering function on perturbations in elastic coefficients
$\mathbf{A}$ = Sensitivity (matrix) of PP-reflection coefficients on fracture weakness
a_N, a_V, a_H etc. = Elements of the sensitivity matrix $\mathbf{A}$
$\mathbf{B}$ = Sensitivity (matrix) of PS-reflection coefficients on fracture weakness
b_N, b_V, b_H etc. = Elements of the sensitivity matrix $\mathbf{B}$
c, a = Aperture and diameter of penny-shaped cracks, respectively
f = (=c/a), aspect ratio of cracks
e = Fracture density
κ, κ' = Incompressibility of rock matrix and fluid infill
s = $(=\kappa'/\kappa)$
q = Fluid indicator in case of cracks interacting with equant porosity
$\bar{\varphi}_P$, $\bar{\varphi}_c$ = Fraction of primary (equant) porosity/crack porosity of total porosity
A_p, A_c = Factors governing the relative dominance of primary and crack porosities in fluid indicator
α = P-wave velocity in isotropic host rock
β = S-wave velocity in isotropic host rock
ν = Poisson's ratio of isotropic host rock

REFERENCES

Angerer, E., 2003, Robust P-wave fracture characterization from wide-azimuth seismic data: 65th Annual International Conference and Technical Exhibition of EAGE, Extended Abstracts, 23–26.

Angerer, E., S. A. Horne, J. E. Gaiser, R. Walters, S. Bagala, and L. Vetri, 2002, Characterisation of dipping fractures using PS mode-converted data: 72nd Annual International Meeting, SEG, Expanded Abstracts, 1010–1013.

Bakulin, A., V. Grechka, and I. Tsvankin, 2000, Estimation of fracture parameters from reflection seismic data-Part I: HTI model due to a single fracture set: Geophysics, **65**, 1788–1802.

Chen, H., R. L. Brown, and J. P. Castagna, 2005, AVO for one- and two fracture set models: Geophysics, **70**, C1–C5.

Fryer, G. J., and L. N. Frazer, 1984, Seismic waves in stratified media: Geophysical Journal of the Royal Astronomical Society, **78**, 691–710.

Gray, D., and K. Head, 2000, Fracture detection in Manderson field: A 3-D AVAZ case history: The Leading Edge, **19**, 1214–1221.

Grechka, V., A. Bakulin, and I. Tsvankin, 2003, Seismic characterization of vertical fractures described as general linear slip interfaces: Geophysical Prospecting, **51**, 117–129.

Grechka, V., and I. Tsvankin, 2004, Characterization of dipping fractures in a transversely isotropic background: Geophysical Prospecting, **52**, 1–10.

Hall, S. A., J. M. Kendall, and O. I. Barkved, 2002, Fractured reservoir characterization using P-wave AVOA analysis of 3D OBC data: The Leading Edge, **21**, 777–781.

Hsu, C. J., and M. Schoenberg, 1993, Elastic waves through a simulated fractured medium: Geophysics, **58**, 964–977.

Hudson, J. A., 1980, Overall properties of a cracked solid: Mathematical Proceedings of the Cambridge Philosophical Society, **88**, 371–384.

———, 1981, Wave speeds and attenuation of elastic waves in material containing cracks: Geophysical Journal of the Royal Astronomical Society, **64**, 133–150.

Hudson, J. A., E. Liu, and S. Crampin, 1996, The mechanical properties of materials with interconnected cracks and pores: Geophysical Journal International, **124**, 105–112.

Jenner, E., 2002, Azimuthal AVO: Methodology and data examples: The Leading Edge, **15**, 782–786.

Liu, E., X. Y. Li, and J. H. Queen, 2001, Discrimination of pore fluids from P- and converted shear-wave AVO analysis, *in* L. Ikelle and A. Gangi, eds., Anisotropy 2000: Fractures, converted waves and case studies: Proceedings of the 9th International Workshop on Seismic Anisotropy, SEG, 203–221.

Luo, M., and B. J. Evans, 2004, An amplitude-based multiazimuth approach to mapping fractures using P-wave 3D seismic data: Geophysics, **69**, 690–698.

Lynn, H. B., W. B. Beckham, K. M. Simon, C. R. Bates, M. Layman, and M. Jones, 1999, P-wave and S-wave azimuthal anisotropy at a naturally fractured gas reservoir, Bluebell-Altamont field, Utah: Geophysics, **64**, 1312–1328.

MacBeth, C., 1999, Azimuthal variation in P-wave signatures due to fluid flow: Geophysics, **64**, 1181–1192.

Mallick, S., and L. N. Frazer, 1991, Reflection/transmission coefficients and azimuthal anisotropy in marine seismic studies: Geophysical Journal International, **105**, 241–252.

Press, W. H., B. P. Flannery, S. A. Teukolsky, and W. T. Vatterling, 1989, Numerical recipes: The art of scientific computing: Cambridge University Press.

Rüger, A., 1997, P-wave reflection coefficients for transversely isotropic models with vertical and horizontal axis of symmetry: Geophysics, **62**, 713–722.

———, 1998, Variation of P-wave reflectivity with offset and azimuth in anisotropic media: Geophysics, **63**, 935–947.

Rüger, A., and I. Tsvankin, 1997, Using AVO for fracture detection: Analysis basis and practical solutions: The Leading Edge, **10**, 1429–1434.

Sayers, C. M., and J. E. Rickett, 1997, Azimuthal variation in AVO response for fractured gas sands: Geophysical Prospecting, **45**, 165–182.

Schoenberg, M., 1980, Elastic wave behavior across linear slip interfaces: Journal of Acoustical Society of America, **68**, 1516–1521.

———, 1983, Reflection of elastic waves from periodically stratified media with interfacial slip: Geophysical Prospecting, **31**, 265–292.

Schoenberg, M., and J. Douma, 1988, Elastic wave propagation in media with parallel vertical fractures and aligned cracks: Geophysical Prospecting, **36**, 571–590.

Schoenberg, M., and C. Sayers, 1995, Seismic anisotropy of fractured rock: Geophysics, **60**, 204–211.

Shaw, R. K., and M. K. Sen, 2004, Born integral, stationary phase and linearized reflection coefficients in weak anisotropic media: Geophysical Journal International, **158**, 225–238.

Shen, F., X. Zhu, and M. N. Toksöz, 2002, Effects of fractures on NMO velocities and P-wave azimuthal AVO response: Geophysics, **67**, 711–726.

Thomsen, L., 1986, Weak elastic anisotropy: Geophysics, **51**, 1954–1966.

———, 1995, Elastic anisotropy due to aligned cracks in porous rock: Geophysical Prospecting, **43**, 805–830.

van der Kolk, C. M., W. S. Guest, and J. H. H. M. Potters, 2001, The 3D shear experiment over the Natih field in Oman: the effect of fracture filling fluids on shear propagation: Geophysical Prospecting, **49**, 179–197.

Williams, M., and E. Jenner, 2002, Interpreting seismic data in the presence of azimuthal anisotropy; or azimuthal anisotropy in the presence of the seismic interpretation: The Leading Edge, **15**, 771–774.

Wu, C., J. M. Harris, K. T. Nihei, and S. Nakagawa, 2005, Two dimensional finite difference seismic modeling of an open fluid-filled fracture: Comparison of thin layer and linear slip models: Geophysics, **70**, T57–T62.

Zhu, P., J. Wang, and G. Zhu, 2004, Inverting reservoir crack density from P-wave AVOA data: Journal of Geophysics and Engineering, **1**, 168–175.